

RSC Advances



This is an *Accepted Manuscript*, which has been through the Royal Society of Chemistry peer review process and has been accepted for publication.

Accepted Manuscripts are published online shortly after acceptance, before technical editing, formatting and proof reading. Using this free service, authors can make their results available to the community, in citable form, before we publish the edited article. This *Accepted Manuscript* will be replaced by the edited, formatted and paginated article as soon as this is available.

You can find more information about *Accepted Manuscripts* in the [Information for Authors](#).

Please note that technical editing may introduce minor changes to the text and/or graphics, which may alter content. The journal's standard [Terms & Conditions](#) and the [Ethical guidelines](#) still apply. In no event shall the Royal Society of Chemistry be held responsible for any errors or omissions in this *Accepted Manuscript* or any consequences arising from the use of any information it contains.

Cite this: DOI: 10.1039/c0xx00000x

www.rsc.org/xxxxxx

ARTICLE TYPE

Multi-Parametric Imaging of Invasiveness-Permissive Acidic Microenvironment in Human Glioma Xenografts

Cuiyun Huang[†], Huan Qin[‡], Jun Qian[†], Jingye Zhang[†], Shengyuan Zhao[†], Yinzhi Changyi[†], Bingbing Li[‡], Jianping Zhang[§], Jianhua Zhu[†], Da Xing[‡], Sihua Yang^{‡**} and Cong Li^{†**}

Received (in XXX, XXX) Xth XXXXXXXXX 20XX, Accepted Xth XXXXXXXXX 20XX

DOI: 10.1039/b000000x

Gliomas, the intrinsic tumors of the brain, are currently incurable because they are extremely invasive. The infiltrated nature of glioma makes them difficult to be completely excised and leads to high recurrence rate. Acidification of extracellular microenvironment plays an important role in the invasion, migration and metastasis of solid tumors. To elucidate the relationship between acidic microenvironment and invasiveness of glioma, multi-parametric imaging studies were conducted between the highly invasive orthotopic (ortho.) human U87MG glioma xenograft and lowly invasive subcutaneous (s.c.) U87MG xenograft. *In vivo* optical imaging showed higher overall acidity of ortho. tumor than that of s.c. tumor after administration of pH responsive near-infrared (NIR) fluorescence probe. Positron emission tomography/computed tomography (PET/CT) imaging demonstrated higher glucose uptake in ortho. tumor after injection of [¹⁸F]-fluorodeoxyglucose (¹⁸F-FDG). Photoacoustic microscopy imaging (PAM) revealed higher vascular density but more aberrant vessel morphology in ortho. tumor. Immunofluorescence microscopic imaging indicated significantly up-regulated acidification associated enzymes in glioma than normal brain tissue. This work not only reveals the acidity correlated glioma invasiveness, but also shows the promise for curbing glioma invasiveness by neutralizing intratumoral acidity via down-regulating glucose uptake, normalizing tumor vasculatures or blocking the acidification associated metabolic/physiological processes.

1. Introduction

Gliomas, the most common and formidable type of primary brain tumors, are currently no cure because of a disproportionate level of mortality worldwide¹. For example, despite of substantial treatments such as maximal surgical resection, conformal radiation and systemic chemotherapy, the median overall survival (OS) is only 14.6 months for patients with glioblastomas multiforme (GBM)², the most aggressive glioma variant. High invasiveness is a dominated reason leading to the poor prognosis of glioma patients. Unlike the normal glial cells whose proliferation, differentiation, and migration are tightly controlled³, the transformed glial cells infiltrate into brain tissue so aggressively that "crab claw-like" or "firework-like" spreading patterns are formed along the white matter track, blood vessels and parenchyma⁴. Due to the infiltrated and heterogeneous nature of glioma cells, it is extremely difficult to completely eliminate the neoplastic tissue, which leads to the high recurrence. Therefore, attenuating the invasiveness of glioma will be helpful to reduce its high invasiveness and mortality.

Acidification of extracellular pH (pH_e) is a universal characteristic of solid tumors regardless of genotype and phenotype⁵. While the pH_e in normal tissues is measured in a range of 7.3–7.4, the value in solid tumors are determined in a range of 6.2–6.9^{6,7}. Tumor acidification plays an important role in maintaining cancer cell invasiveness^{6,7} by up-regulating tumorigenic transformation⁴, promoting angiogenesis³, accelerating extracellular matrix (ECM) remodeling⁸, resisting chemotherapy⁹ and suppressing the immune response¹⁰. For example, cancer cells exposed to *in vitro* low pH performed increased invasive tendency¹¹ and regions of highest tumor invasion usually corresponded to areas of lowest pH¹². The proton concentration gradient from the tumor to adjacent normal tissue promotes tissue remodeling at the tumor-stroma interface^{13,14} and increases activities of proteases such as cathepsin¹¹, which is actively involved in local invasion. Furthermore, neutralization of intratumoral acidosis with systemic buffers such as bicarbonate inhibited tumor local invasion^{15,16}. Based on above experimental results, we hypothesize that the acidic microenvironment plays an important role in maintaining the high invasiveness of glioma. Evaluating acidity and acidity associated physiological/metabolic processes will help to understand the acidification correlated invasiveness and hence identify potential therapeutic targets for glioma treatment.

To support the rapid growth and proliferation, cancer cells metabolize glucose through glycolysis¹⁴ instead of oxidative phosphorylation used in normal cells in the presence or absence of oxygen supplies. This phenomenon was first described by Warburg about 80 years ago and named as "Warburg effect"¹⁵. A large amount of lactic acid as the ending product of glycolysis is believed to be the main reason leading to extracellular acidity. For example, experimentally induced hyperglycemia acidified tumor pH_e from 7.4 to 6.7 coincident with an increase in the glycolytic rate¹⁷. Glycolysis relies on a series of enzymes to metabolize glucose to lactic acid (Figure 1). They include the facultative glucose transporter 1 (GLUT1) that increases the intracellular glucose

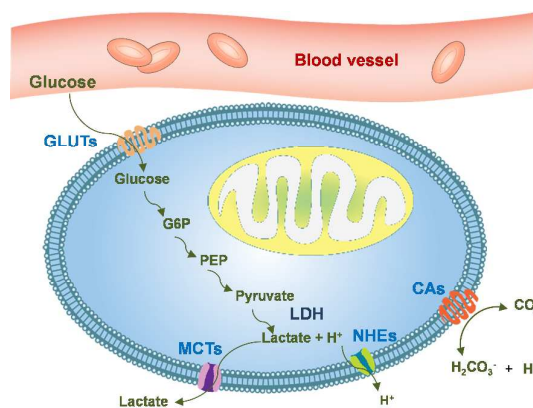


Figure 1. Key enzymes/membrane ion channel proteins involved in tumor acidification. Acidification is associated with fermentative glycolysis that produces excess lactic acid, increased activities of membrane proton transporters such as Na^+/H^+ exchangers (NHEs) that accelerate intracellular proton efflux and carbonic anhydrases (CAs) that catalyze hydration of extracellular CO_2 to carbonic acid. Up-regulated glycolysis is characterized by enhanced glucose uptake via glucose transporters (GLUTs), conversion of glucose to lactate and H^+ via lactate dehydrogenase (LDH) and increased efflux of lactic acid via monocarboxylate transporters (MCTs).

uptake rate^{18,19}, lactate dehydrogenase (LDH) that converts the pyruvate into lactate^{20,21}, monocarboxylate transporter 4 (MCT-4) that exports lactate out of the cells²⁰. Besides the glycolysis, tumor acidity is also maintained by up-regulation of plasma membrane ion transporters such as Na^+/H^+ exchanger (NHE)²² that effluxes the proton to extracellular fluid and carbonic anhydrase 9 (CA9) that accelerates the hydration of extracellular CO_2 to H^+ and HCO_3^- ²¹. Besides the metabolic alternations, tumor acidity was also reported to contribute from the poor diffusion rate that prevents the timely drainage of proton¹². Bullitt et al quantitatively measured vessel attributes including vessel density, radius, tortuosity and terminal branch degree within five types of gliomas by high-resolution magnetic resonance imaging (MRI)²³. Compared to normal brains, all glioma patients demonstrated the marked increase in vessel tortuosity and terminal branch count. Therefore, studying fermentative glycolysis, acidification associated enzymes/transporters and vascular morphology help to understand the acidosis associated invasiveness in glioma.

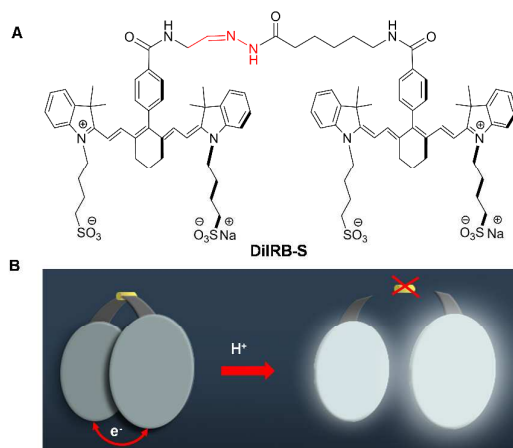
Previous works demonstrated that while orthotopic glioma xenografts showed high invasiveness including widespread dissemination, infiltration along white matter tracts, seeding of the ventricular system and extension along the leptomeninges, subcutaneous xenografts possessing glioma characteristic receptors such as epidermal growth factor receptor (EGFR) lost their invasiveness by forming discrete mass with well-circumscribed border that pushed aside rather than invade adjacent normal tissue²⁴. In this work, mouse models inoculated both ortho. human U87MG glioma xenograft and s.c. U87MG glioma xenograft were developed to investigate the relationship between acidity and invasiveness of glioma. Because molecular imaging shows the promise in monitoring biological events in molecular and cellular levels

with high sensitivity and spatial resolution, multiparametric imaging strategies were used to compare acidity and acidity associated physiological processes between ortho. and s.c. glioma xenografts. Acidity in tumor was determined by *in vivo* optical imaging after intravenous (*i.v.*) administration of home-made pH responsive near-infrared fluorescence probe **DiIRB-S**²⁵. Glucose uptake efficiency was evaluated by *in vivo* positron emission tomography/computed tomography after *i.v.* injection of radioactive glucose derivative [¹⁸F]-fluorodeoxyglucose. Vascular density and morphology in tumor margin areas were imaged by *in vivo* photoacoustic microscopy imaging. Additionally, the expression levels of acidity associated enzymes/transporters were evaluated by *ex vivo* immunofluorescence microscopic imaging. Overall, this work not only elucidates the relationship between glioma acidity and its invasiveness, but also helps to identify glioma treatment by blocking tumor acidity or acidity associated physiological/metabolic pathways.

2. Results

2.1 pH responsive NIR fluorescence and photoacoustic probe

In previous work, we developed a pH responsive NIR fluorescence probe **DiIRB-S** that showed the capability to visualize intratumoral acidosis²⁶. In this probe, two NIR fluorophores with high photochemical stability and extinction coefficient were conjugated via an acid liable hydrazone bond. Under neutral pH, the fluorophores formed a face to face H-type aggregate through Van der Waals force and their fluorescence was suppressed efficiently (Scheme 1). The cleavage of acid liable bond in acidic pHs with concomitant aggregate disruption resulted in substantial fluorescence enhancement. **DiIRB-S** exhibited two absorption bands at 686 and 756 nm in aqueous solution, which were assigned to the H-type aggregate and fluorophore monomer²⁷ (Figure 2A, Figure S1A–C). Notably, while absorbance at 756 nm (A_{756}) increased consistently at pH 5.5, absorbance at 686 nm (A_{686}) decreased gradually, which indicated the conversion of the aggregate to monomer under acidic environment. Time course of the absorbance ratio A_{756}/A_{686} was further measured at pH 7.4, 6.5 and 5.5 that mimicks the environment of normal tissues, tumor extracellular fluid and lysosomal compartment. The hydrolytic velocities of the aggregate under pH 5.5 and 6.5 were about 52.6 and 13.2 times faster than that under pH 7.4 (Figure 2B). Fluorospectroscopy studies demonstrated that the fluorescence intensity of **DiIRB-S** centered at 778 nm increased as many as 22.6 times in the first 2 h after incubation at pH 5.5 (Figure 2C, Figure S1D–F). Time dependent fluorescence intensity of **DiIRB-S** indicated that the signal enhancement velocities at pH 5.5 and 6.5 were 17.0 and 7.1 times higher than that under pH 7.4 in the first 2 h post-incubation (Figure 2D). Similar to absorption spectra, while the photoacoustic signal excited at 686 nm decreased consistently (Figure 2E, Figure S2A–C), the signal excited at 756 nm increased gradually at pH 5.5 (Figure S2D–F). Figure 2F demonstrated time dependent PA signal ratio (PA_{756}/PA_{686}) of **DiIRB-S** in the first 2 h after incubation under pH 7.4, 6.5 and 5.5. The slopes of fitting straight lines between incubation time and PA_{756}/PA_{686} ratio correlated to the acidity



Scheme 1. pH responsive NIR fluorescence probe **DiIRB-S** evaluating tumor acidity. (A) Chemical structure of **DiIRB-S**. The acid liable hydrazone bond is indicated by red color. (B) Cartoon presenting fluorescence enhancement mechanism of **DiIRB-S** under acid pHs.

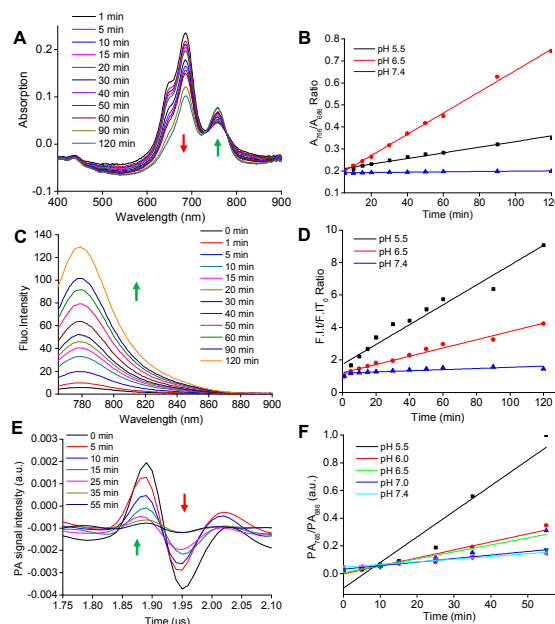


Figure 2. **DiIRB-S** determines pH values by acidity correlated absorption, emission and photoacoustic signal variation velocities. Time dependent absorption spectra (1.0 μ M) at pH 5.5 (A) and time courses of absorption ratio A_{756}/A_{686} (B) at pH 7.4, 6.5 and 5.5. Time dependent emission (1.0 μ M) under pH 5.5 (C) and time courses of fluorescence intensities (D) at above three pHs (excited at 756 nm). Time dependent photoacoustic spectra (1.0 μ M) under pH 5.5 (excited at 756 nm) (E) and time courses of photoacoustic signal ratio PA_{756}/PA_{686} (F) at pH 7.4, 7.0, 6.5, 6.0 and 5.5.

of the buffer solutions. The slopes measured at pH 5.5 and 6.5 were 9.5 and 2.6 times higher than the value measured at pH 7.4.

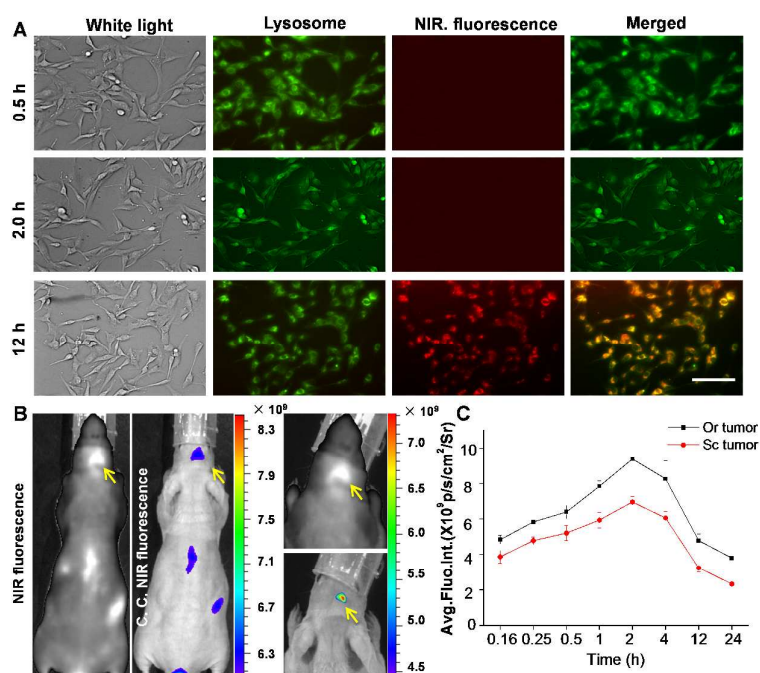


Figure 3. Ortho. glioma xenograft showed higher overall acidity than s.c. glioma xenograft. (A) Fluorescence microscopic images of live U87MG cells treated with **DiIRB-S** (25 μM) in a media with pH 6.5 for selected incubation times. The fluorescence of lyso-tracker was displayed in green and the NIR fluorescence was displayed in red. Bar = 50 μm . (B) Representative *in vivo* NIR fluorescence images of mouse bearing ortho. glioma xenograft at 2 h PI of **DiIRB-S** (40 nmol/mouse), unit: $\text{p/s/cm}^2/\text{Sr}$. Arrows point to the tumor position; (C) Time dependent NIR fluorescence intensities on the tumors after injection of **DiIRB-S** via i.v.. Data are presented as mean \pm SD ($n = 4$ mouse models bearing both ortho. and s.c. tumor xenografts). C.C. = color coded.

2.2 Ortho. tumor showing higher gross acidity than s.c. tumor

Besides the tumor extracellular fluid, acidosis also exists in the lysosomes of cancer cells. To verify the activation of **DiIRB-S** in tumor extracellular matrix rather than the lysosomes²⁸, the cultured U87MG cells were treated with **DiIRB-S** (25 μM) for 0.5, 2.0 or 12 h in a media (pH 6.5) mimicking the tumor extracellular environment (Figure 3A). While the probe signals were not detected after incubation for 0.5 and 2.0 h, the signals as small vesicular structures were observed at 12 h post treatment and they colocalized well with the lysosomes stained by lyso-tracker, which indicates that lysosomes are the intracellular delivering destination of the probe. Therefore, **DiIRB-S** actually senses acidosis in tumor extracellular fluid but not the lysosomes if the imaging studies are conducted within 2 h after the probe treatment. **DiIRB-S** (40 nmol/mouse) successfully visualized both ortho. and s.c. glioma xenografts with significant NIR fluorescence enhancement at 2 h after intravenous injection of the probe (Figure 3B). Ortho. and s.c. tumors demonstrated similar time courses of NIR fluorescence intensity. The fluorescence signal in both types of tumor increased substantially and reached their maximum as 8.3 ± 1.3 and $6.4 \pm 0.4 \times 10^9$ $\text{p/s/cm}^2/\text{Sr}$ (mean \pm SD, $n = 4$) at 2 h post-injection (PI) (Figure 3C). The signals of both tumors decreased after reaching the maximal values and the minimal values were observed at 24 h PI. However, the fluorescence intensities on ortho. tumor

were higher than those of s.c. tumor during the whole imaging process, which implied the higher gross acidity of the extracellular fluid in ortho. tumor.

2.3 Ortho. tumor showing rapider glucose uptake than s.c. tumor

Figure 4A showed the representative 2D projection of *in vivo* microPET/CT images of a mouse model bearing both ortho. and s.c. glioma xenograft at 0.5 and 3.5 h PI of ¹⁸F-FDG (11 MBq/mouse). Prominent uptakes in both types of tumors, kidneys, intestinal tract, urinary bladder and brain were clearly observed at 0.5 h PI. Radioactivity accumulation was observed in normal brain tissues, especially in the cerebellum, which led to the compromised T/B ratio (1.19 ± 0.05) of the ortho. tumor (mean \pm SD, $n = 3$). The radioactivity in normal brain tissues decreased with time after FDG injection, which resulted in the increased T/B ratio of ortho. tumor (2.26 ± 0.10) at 3.5 h PI. Notably, in the s.c. tumor, the radioactivity initially located in the core area but extended to whole tumor at 3.5 h PI. Figure 4B presented *in vivo* standardized uptake value (SUV) of ortho. and s.c. tumors at selected time-points PI of ¹⁸F-FDG. The minimal SUV values of both ortho. (1.63 ± 0.07) and s.c. tumors (1.25 ± 0.14) were found at 3.0 min after ¹⁸F-FDG injection. The SUV of ortho. tumor reached its maximal value 2.03 ± 0.09 at 2 h PI. In contrast, the SUV of s.c. tumor increased more rapidly and its maximum (2.10 ± 0.06) was recorded at 1 h PI. The SUV of both ortho. and s.c. tumor decreased after reaching their maximums and their values were determined as 1.76 ± 0.10 and 1.89 ± 0.08 respectively at 3.5 h PI. *In vivo* bio-distribution data

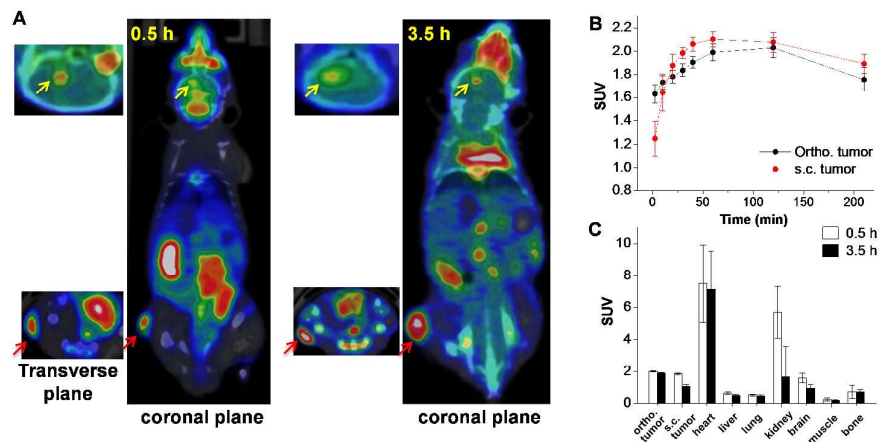


Figure 4. Ortho. glioma xenograft showed rapid uptake of radioactive glucose derivative ^{18}F -FDG than s.c. glioma xenograft. (A) Representative in vivo PET/CT images of mouse model bearing both ortho. and s.c. glioma xenografts at 0.5 h and 3.5 h PI of ^{18}F -FDG (11 MBq/mouse) via i.v.. Inserted pictures offered the coronal position of ortho. and s.c. tumors that were pointed out by yellow and red arrows respectively. (B) Time course of SUVs in ortho. and s.c. tumors after administration of ^{18}F -FDG via i.v.. (C) In vivo bio-distribution of ^{18}F -FDG in glioma xenografts and main organs at 0.5 and 3.5 h PI. Data were presented as mean \pm SD ($n = 3$ mouse models bearing both ortho. and s.c. tumor xenografts).

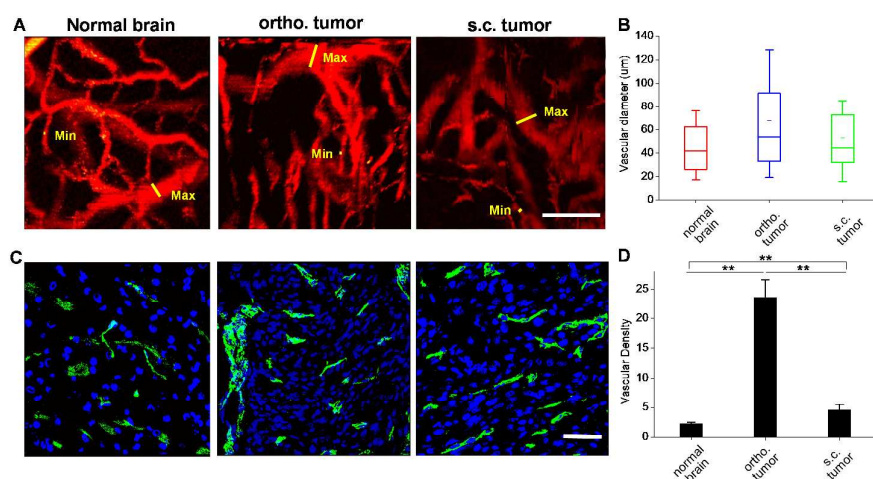


Figure 5. Ortho. tumor showed more variable vessel diameter and higher vascular density than s.c. tumor and normal brain tissue. (A) Representative in vivo PAM images of vasculatures in normal brain, margin areas of ortho. and s.c. tumors. Yellow lines indicate vessels with maximal and minimal diameters in the field of view (excited at 532 nm). Bar: 200 μm . (B) Vascular diameters in normal brain, margin area of ortho. and s.c. tumor. (C) Microscopic fluorescence images of normal brain, ortho. and s.c. tumor margin immuno-stained by CD31 antibody. The nuclear stained by DAPI was displayed in blue and immunofluorescence presenting vessels was displayed in green. Bar: 50 μm . (D) Vascular densities in normal brain, ortho. and s.c. tumor xenografts. Data were presented as mean \pm SD ($n = 12$ slides from 3 mouse models bearing both ortho. and s.c. tumor xenografts). **, $P < 0.01$.

demonstrated the highest SUV values in the heart in either 0.5 h (7.50 ± 2.4) or 3.5 h (7.13 ± 2.2) after FDG injection. While the SUV in kidney, brain and s.c. tumor decreased remarkably, the values in heart and ortho. tumor were barely changed from 0.5 to 3.5 h PI (Figure 4C).

2.4 Ortho. glioma showing more aberrant vascular morphology than s.c. tumor

Figure 5A demonstrated the *in vivo* photoacoustic microscopy (PAM) images of vasculatures in the normal brain, margin areas of ortho. and s.c. glioma xenograft. Vasculatures in

normal brain formed a well-organized and regulated architecture, but tumor vasculatures lost the conventional hierarchy and were highly disorganized, tortuous, characterized with inconsistent diameter and uneven shape with abnormal bulges and blind ends. While the vessel diameters in normal brain tissue were determined in a range of 17.2–76.3 μm , broader diameter distribution were measured in ortho. tumor (19.1–128.4 μm) and s.c. tumor (15.8–85.2 μm) (Figure 5B). The average vessel diameter of ortho. tumor was measured as 67.7 μm that was higher than s.c. tumor (51.1 μm) as well as normal brain tissue (47.4 μm). Figure 5C demonstrated the

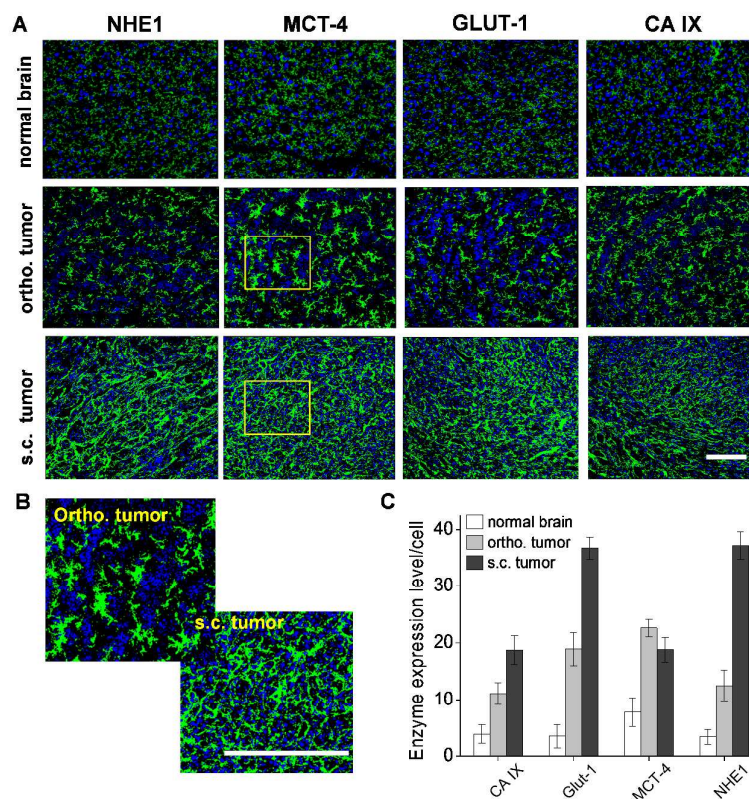


Figure 6. Expression level of acidity associated enzymes/ion channel proteins. (A) Representative microscopic immunofluorescence images of normal brain, ortho. and s.c. tumor sections. The nuclei stained by DAPI were displayed in blue and immunofluorescence was displayed in green. (B) Enlarge pictures of MCT4 immunofluorescence images highlighted in the yellow boxes of panel A. (C) Average immunofluorescence intensity per cell in normal brain, ortho. and s.c. tumors. Data were presented as mean \pm SD ($n = 12$ slides from 3 mouse models). Bar: 50 μm .

microscopic fluorescence images of normal brain and glioma sections, in which the vessels were immunohistochemically stained by CD31 antibody. Compared to the normal brain tissue, the nuclei in tumor margins distributed with higher density, which presents the fast proliferation rate of glioma cells. Similar to *in vivo* photoacoustic imaging, the vessels in both ortho. and s.c. tumors showed aberrant morphology such as heterogeneous diameters, uneven shape and blind ends. Additionally, microvessel density (MVD) of ortho. tumor was measured as 6.3 and 3.2 times higher than normal brain tissue and the s.c. tumors (Figure 5D).

2.5 Both types of glioma showing higher expression levels of acidity associated enzymes

Ex vivo immunofluorescence microscopic imaging was conducted to evaluate the expression level of acidity associated enzymes in normal brain tissues and invasive edges of glioma xenografts. As shown in Figure 6A, acidity associated enzymes including GLUT1, NHE1, MCT4, CA9 were clearly observed in the normal brain tissues and they located as tiny vesicular structures in the cytoplasm. Compared to normal brain tissues, all above enzymes were over-expressed in both ortho. and s.c. tumors. In ortho. tumor, the enzymes distributed as star-like cluster structures extended from the peri-nuclei area to the extracellular space. In s.c. tumors,

these enzymes located as stripe-like structures filled in whole intracellular and extracellular space. The enlarged MCT4 immunofluorescence images clearly showed the different distribution patterns between ortho. and s.c. tumors (Figure 6B). Figure 6C demonstrated the immunofluorescence intensities of these enzymes in normal brain, ortho. and s.c. tumor. Obviously, s.c. tumor demonstrated the highest expression levels of GLUT1, NHE1, CA9 that were averagely 10.4, 10.9 and 4.8 times higher than those of normal brain. The highest expression level of MCT4 was detected in ortho. tumor and it was 2.9 times higher than that of normal brain.

3. Discussion

Magnetic resonance imaging (MRI) technologies such as MR spectroscopy imaging (MRSI)⁷ and chemical exchange saturation transfer (CEST) MRI^{29, 30} have been used to determine pH values in solid tumor. However, due to the inherently low sensitivity of MRI, high dose of imaging agents (0.1–10 mM) and long acquisition time (min–hr) are inevitable. Compared to MRI, optical imaging demonstrates high sensitivity, fast response rate and convenience for manipulation³¹. NIR fluorescence imaging shows advantages for *in vivo* studies because NIR light with wavelengths in a

range of 650–900 nm performs low phototoxicity, minimized absorption and autofluorescence from endogenous tissues, which allows it to visualize biological events in deep tissues ($< 1.0 \text{ cm}$)³¹. We previously developed a series of pH response NIR fluorescence probes to image tumor^{32,33} or evaluate tumor metastatic potentials^{25, 34} by sensing acidic tumor microenvironment (TME). In this work, **DiIRB-S** was chosen to evaluate glioma invasiveness because of its predominant signal activation in tumor extracellular fluid. This capability of **DiIRB-S** could be explained by its remarkable pH responsive fluorescence enhancement and overall negative charge that prevents the efficient intracellular delivery into the acidic lysosomes.

PAM is a non-invasive imaging modality that detects optical absorption contrast by collecting the acoustic signal generated via photoacoustic effect³⁵. As an emerging imaging technology, PAM combines advantages of high sensitivity of optical imaging and spatial resolution of ultrasonic imaging³⁶. By using NIR fluorophore as the imaging probe, PAM successfully detected objects embedded at depths of as much as 5.2 cm in chicken breast muscle with a resolution of $< 780 \mu\text{m}$ and a sensitivity of $< 7 \text{ pmol}$ probe in blood³⁷. Considering the pH correlated time dependent $\text{PA}_{756}/\text{PA}_{686}$ ratio of **DiIRB-S**, it is possible to determine local pH values in glioma after systemic injection of this probe.

Compared to oxidative phosphorylation (36 ATP/glucose), glycolysis is a low efficient glucose metabolic pathway to generate energy molecules (4 ATP/glucose)³⁸. Due to metabolic alternation from oxidative phosphorylation to aerobic glycolysis in cancer cells, tumors have to elevate glucose consumption to compensate the low efficiency of glycolysis. Increased glucose uptake as a characteristic of glycolysis has been used to evaluate tumor malignancy. For example, Di Chiro et al first showed that there was a positive correlation between glioma malignancy and glycolytic activity in clinical studies³⁹. High grade gliomas with high glycolytic level demonstrated a much stronger radiotracer ^{18}F -FDG (glucose analogue) uptake than low grade gliomas with low glycolytic level. Therefore, it is possible to evaluate glycolytic level and invasiveness by quantify ^{18}F -FDG signal intensity in ortho. and s.c. tumor. SUV defined as ^{18}F -FDG retention normalized to injected dose and tissue weight is an established index for quantifying glucose metabolic activity in tissue. As shown in Figure 4, much higher SUV of ortho. tumor than s.c. tumor in the first 5 min PI of ^{18}F -FDG injection implied the higher glycolytic level in ortho. tumor. Lodge et al reported that the high-grade gliomas cost a longer time to reach the maximal FDG uptake value than that of the benign lesions⁴⁰. Compared to s.c. tumor, ortho. tumor need one more hour to reaching the maximum of SUV, which indicates higher malignancy/ invasiveness of ortho. tumors than s.c. tumor.

The vasculatures in the high-grade gliomas were typified as characteristics such as hyperpermeability, high vessel density, inconsistent diameters, unidentified arterioles and venules, tortuous shape with abnormal bulges and blind ends^{41, 42}. Imaging micro-vasculatures in glioma xenografts also helps to elucidate the invasiveness of gliomas. Even MRI offers high spatial resolution to visualize tumor vasculatures, it

is still difficult to detect the vasculatures with a diameters less than $100 \mu\text{m}$ ⁴³. Because PA signal intensity usually correlates to its optical absorption, much higher extinction coefficient of hemoglobin at 532 nm (200 cm^{-1}) than other endogenous molecules such as epidermis (20 cm^{-1}) or dermis (0.4 cm^{-1}) provides its feasibility to non-invasively monitor micro-vasculatures that are hardly to be detected by MRI⁴⁴. For example, PAM visualized vasculatures in mouse ear with a lateral resolution as high as $0.5 \mu\text{m}$ under *in vivo* condition⁴⁵. As shown in Figure 5A, PAM demonstrated the highest vascular density and the most aberrant vascular morphology in ortho. glioma xenograft. The heterogeneous vasculatures may accelerate the tumor acidity and invasiveness by following explanations: 1. the poor oxygenation increases glucose metabolism via glycolytic pathway and produces more lactic acid⁴¹; 2. the limited perfusion rate hampers the drainage of the metabolized proton, which inevitably results in acidification of local micro-environment; 3. the structural abnormalities of tumor vasculatures lead to spatial and temporal heterogeneity in tumor blood flow, which elevates interstitial fluid pressure and pushes fluid flow from the tumor margin into the peri-tumor area and finally facilitates peri-tumor invasion by acidifying local extracellular fluid^{24, 46}. Therefore, ‘normalization’ of aberrant structure and function of tumor vasculatures will make them more efficient for oxygen delivery and then decrease the acidity and invasiveness of glioma.

Compared to normal brain tissues, all four acidity associated enzymes tested in this work were up-regulated in both types of glioma xenografts, which partially explained the higher extracellular acidity in tumor. Interestingly, in these enzymes, only MCT4 showed its highest expression level in ortho. tumor. Previous work showed that MCTs induce intracellular acidification by efflux of excess lactic acid out of the cytoplasm. Baltazar et al reported that MCT1 and MCT4 were over-expressed in the plasma membrane of glioblastomas and MCT1 inhibitors exhibited anti-tumoral and antiangiogenic activity⁴⁷. As a potential therapeutic target, down-regulation of MCTs may attenuate acidic microenvironment and limit gliomas invasiveness.

4. Experimental

4.1 Materials. Rabbit anti-mouse CD31 primary antibody was purchased from Abcam (Cambridge, UK). Rabbit anti-mouse CA9, GLUT1, MCT4 and NHE1 primary antibody were purchased from Santa Cruze Biotechnology (California, USA). Alexa Fluor 488-labeled goat anti-rabbit secondary antibody was purchased from Cell Signaling Technology (Danvers, USA). DAPI was purchased from sigma (St. Louis, USA). ^{18}F -FDG was produced automatically by a cyclotron (RDS Eclips ST; Siemens) and an Explora FDG4 module (Siemens) in Fudan University Shanghai Cancer Center. Human glioblastoma U87MG cells were purchased from Chinese Academy of Science Cell Bank. Lysosome Tracker was purchased from Life Technology (Eugene, USA)

4.2 Methods. All absorption spectra were recorded on a HIMADZU UV-2550 spectrophotometer. All fluorescence

spectra were recorded on SHIMAZDU RF-5301PC spectrophotometer. All pH measurements were performed with a Mettler Toledo MP220 pH meter equipped with a Mettler Toledo InLab® glass electrode. *In vivo* and *ex vivo* NIR fluorescence images were acquired in IVIS Spectrum *In Vivo* Imaging System (Cailper Perkin Elemer, USA). *In vivo* photoacoustic microscopic images were collected from home-made system equipped with an Nd:YAG laser, operating at the wavelength of 532 nm with a full-width at high magnitude (FWHM) of 4.0 ns and a repetition of 20 Hz. Meanwhile, a tunable pulsed laser source (Surelite OPO Plus, USA) was applied with wavelengths in a range of 675–100 nm, a pulse width of 4–6 ns, and a pulse repetition rate of 20 Hz. *In vivo* PET/CT imaging was performed on an Inveon system (Siemens, Germany) after intravenous injection of ^{18}F -FDG. Live cell fluorescence microscopic images were collected on a Leica DMF4000B laser-scanning microscope (Leica Inc, Germany) inverted microscope with epifluorescence by using 20× objective lenses. The Lyso-tracker was excited by a N3 filter (546 ± 6 nm) and its emission was collected with a 600 ± 20 nm band-pass filter. Meanwhile, DiIRB-S was excited by a Y7 filter (710 ± 37.5 nm) and its emission was detected by a 810 ± 45 nm band-pass filter. The immunofluorescence images were collected on a Zeiss LSM 710 META confocal laser scanning microscope (Carl Zeiss, Germany) by using a 20X lens. DAPI was excited with a 405 nm laser and the emission was detected with a photomultiplier by a 420–480 nm band-pass filter. Alexa-Flour488 was excited with a 488 nm laser and emission was detected by a second photomultiplier using a 505–550 nm band-pass filter.

4.3 pH dependent spectroscopic studies. The stock solution was prepared by dissolving DiIRB-S (9.1 mg, 5×10^{-6} mol) in anhydride dimethyl sulfoxide (DMSO) with a concentration of 10 mM. Working solution of DiIRB-S was prepared by diluting stock solution to buffers with a final concentration of 1.0 μM . Absorption profiles of DiIRB-S working solution were measured under pH 7.4, 6.5 and 5.5 at selected time points after incubation. The scanning speed was 0.5 nm/s and the slit width was set to 2 nm. Emission spectra of DiIRB-S working solution with pH 7.4, 6.5 and 5.5 were excited at 745 nm and collected at selected time points after incubation. For photoacoustic spectroscopic studies, laser beam (excited at 686 nm and 756 nm) was focused to illuminate the working solutions of DiIRB-S in a 0.5 mm diameter glass tube and the PA signals were received by ultrasonic transducer. The PA signal profiles of the working solution with pH 7.4, 7.0, 6.5, 6.0 and 5.5 were obtained at different time points after incubation. Each PA signal was generated by averaging data from 128 times scanning.

4.4 Live cell fluorescence microscope imaging. Human glioblastoma U87MG cells (1.0×10^4) cultured in a 24 well-plate with approximately 50% confluence were treated with 25 μM DiIRB-S for 0.5, 2.0 or 12 h in 1.0 mL DMEM media (pH 6.5) supplemented with 10% FBS and 1% penicillin/streptomycin at 37 °C. After lysosome staining with Lyso-tracker (500 nM), the cells were washed 3× with PBS

prior to microscopy imaging.

4.5 Tumor model development. U87MG cells grown as mono-layers in 75 cm² flasks were cultured at 37 °C and 5% CO₂ in high-glucose DMEM (Hyclone) containing 10% FBS and 1% penicillin/streptomycin. Male nude mice were purchased from Hua Bukang BioTek (Beijing, China) at 4–5 weeks of age and maintained under standard housing conditions. All animal experiments were carried out in accordance with guidelines approved by the Ethics Committee of Fudan University. U87MG cells (5.0×10^6 cells suspended in 150 μL PBS) were inoculated into the right thigh of nude mice. U87MG cells (1×10^6 suspended in 3.0 μL PBS) were injected in corpus striatum at 4–6 days after subcutaneous inoculation. After brain inoculation for 20 days, the mice bearing both ortho. and s.c. glioma xenografts were ready for imaging experiments.

4.6 *In vivo* micro PET/CT imaging studies. The tumor bearing mice after fasting for 8 h were anesthetized by isofluorine and then underwent dynamic PET/CT imaging after i.v. injection of ^{18}F -FDG (11 MBq/mouse). Whole body PET was first performed with 350–650 keV energy window and 3.432 timing window. CT scanning covering the identical transverse field of view was obtained and the PET imaging datasets were reconstructed iteratively by application of the CT data for attenuation correction and co-registration. The PET/CT images were analyzed on Host IAW workstation with Inveon Research Workplace software. An elliptic volume of interest (VOI) was drawn manually around areas with abnormal ^{18}F -FDG uptake to calculate SUV peak (the hottest spot in the tumor foci).

4.7 *In vivo* optical imaging. NIR fluorescence images were acquired by using an Integrin 750 filter set (excitation filter: 745 nm; emission filter: 800–840 nm) after systemic injection of DiIRB-S (40 nmol/mouse). The mice were anesthetized by isoflurane and placed in imaging plate with a position to visualize both ortho. and s.c. glioma xenografts at the same time. At the end of imaging, the mice were scarified and perfused with saline followed 4% paraformaldehyde (PFA) via heart to douche blood and pre-fix the mouse. Brain, subcutaneous tumor and main organs were isolated, imaged and the fluorescence intensities of isolated organs were quantified respectively.

4.8 *In vivo* photoacoustic microscopic imaging. *In vivo* PAM imaging of blood vessels in normal brain tissue and invasive margin of tumors were conducted in mouse models after anesthesia (10% chloral hydrate, 85 μL / mouse). A field flattening lens with magnification of 4X were used to scan a region with diameter of 1.0 mm. An Nd: YAG laser (Surelite II-20, Continuum, USA), operating 4–6 ns pulses at a 532 nm wavelength with a repetition rate of 20 Hz, was used as the light source. A tunable pulsed laser with a repetition rate of 20 Hz and a pulse width of 4 ns (Nd:YAG Surelight-II-20

connected to Surelite OPO Plus, Spectral tuning range 675-1000 nm, Continuum) was used as the light source. The light was scanned by a 2D scanning galvanometer (6231 H, Cambridge Technology) and focused by the objective lens to irradiate the tested tissues. An unfocused ultrasound transducer with center frequency of 15 MHz and -6 dB bandwidth was used to receive the PA signals generated by the tested sample. A silicon photodiode (ET 2000, Electro-Optics Technology, Inc., USA) was used to monitor and calibrate the intensity and stability of the laser beam. The PA signals were recorded through the signal amplifier and a dual-channel data acquisition card. The blood vessel of tumor xenograft was imaged by PAM under 532 nm.

4.9 Immunofluorescence microscopic imaging. Tumor bearing mice were sacrificed and perfused with saline followed 4% PFA via heart to douche blood. The isolated brains and s.c. tumors were fixed in formalin for 12 h, 30% sucrose solution for 24 h and then sectioned coronally with a thickness of 10 μ m. The brain and s.c. tumor sections were stained by primary antibody including MCT4, GLUT1, NHE1, CA9 respectively with a 1:100 dilution. After washing in PBS, the slides were further stained by Alexa fluor 488-conjugated goat anti-rabbit secondary antibody (1:500 dilutions). Confocal fluorescence microscopic images were captured in Laser confocal living cell imaging system (Carl Zeiss LSM710) equipped with a 20X objective lens. The fluorescence intensities/ cell were quantified by ImageJ (NIH, Bethesda, MD) software (n = 8).

4.10 Statistics. Values are presented as the mean \pm SD when the sample number was above 4 (n > 4).

5. Conclusion

Overall, by using multi-parametric imaging technologies, we verified the positive correlation between intratumoral acidity and glioma invasiveness. It is promising for curbing glioma invasiveness by directly neutralizing intratumoral acidity or blocking the acidification associated physiological incidents such as aerobic glycolysis, vascular heterogeneity and over-expression of acidity associated enzymes/transporters.

Acknowledgements

This work is financially supported by the National Basic Research Program of China (973 Program, 2011CB910404, 2013CB932500), the National Natural Science Foundation of China (Nos. 81171384, 81371624), New Century Excellent Talents in University Award and Special Nano-Projects of Shanghai Science and Technology Committee (13NM1400400).

Notes and References

[†]Key Laboratory of Smart Drug Delivery, Ministry of Education, School of Pharmacy, Fudan University, Shanghai, 201203, China, Fax: +86 21 5198 0001, Email: congli@fudan.edu.cn;

[‡]Key Laboratory of Laser Life Science and Institute of Laser Life Science, Ministry of Education, College of Biophotonics, South China Normal University, Guangzhou, 510613, China; Fax: +86 20 8521 6052, Email: yangsh@sfnu.edu.cn

[§]Center for Biomedical Imaging, Department of Nuclear Medicine, Fudan University Shanghai Cancer Center, Fudan University, Shanghai, 200032, China.

- 1 P. Y. Wen and S. Kesari, *N. Engl. J. Med.*, 2008, **359**, 492.
- 2 R. Stupp, W. P. Mason, M. J. van den Bent, M. Weller, B. Fisher, M. J. Taphoorn, K. Belanger, A. A. Brandes, C. Marosi, U. Bogdahn, J. Curschmann, R. C. Janzer, S. K. Ludwin, T. Gorlia, A. Allgeier, D. Lacombe, J. G. Cairncross, E. Eisenhauer, R. O. Mirimanoff, R. European Organisation for Treatment of Cancer Brain, G. Radiotherapy and G. National Cancer Institute of Canada Clinical Trials, *N. Engl. J. Med.*, 2005, **352**, 987.
- 3 N. J. Abbott, L. Ronnback and E. Hansson, *Nat. Rev. Neurosci.*, 2006, **7**, 41.
- 4 A. Giese, *Acta Neurochir. Suppl.*, 2003, **88**, 153.
- 5 P. Friedl and K. Wolf, *Nat. Rev. Cancer*, 2003, **3**, 362.
- 6 B. A. Webb, M. Chimenti, M. P. Jacobson and D. L. Barber, *Nat. Rev. Cancer*, 2011, **11**, 671.
- 7 R. van Sluis, Z. M. Bhujwalla, N. Raghunand, P. Ballesteros, J. Alvarez, S. Cerdan, J. P. Galons and R. J. Gillies, *Magn. Reson. Med.*, 1999, **41**, 743.
- 8 A. F. Chambers and L. M. Matrisian, *J. Natl. Cancer Inst.*, 1997, **89**, 1260.
- 9 Z. M. Bhujwalla, C. L. McCoy, J. D. Glickson, R. J. Gillies and M. Stubbs, *Br. J. Cancer*, 1998, **78**, 606.
- 10 K. Fischer, P. Hoffmann, S. Voelkl, N. Meidenbauer, J. Ammer, M. Edinger, E. Gottfried, S. Schwarz, G. Rothe, S. Hoves, K. Renner, B. Timischl, A. Mackensen, L. Kunz-Schughart, R. Andreesen, S. W. Krause and M. Kreutz, *Blood*, 2007, **109**, 3812.
- 11 E. K. Rofstad, B. Mathiesen, K. Kindem and K. Galappathi, *Cancer Res.*, 2006, **66**, 6699.
- 12 V. Estrella, T. Chen, M. Lloyd, J. Wojtkowiak, H. H. Cornnell, A. Ibrahim-Hashim, K. Bailey, Y. Balagurunathan, J. M. Rothberg, B. F. Sloane, J. Johnson, R. A. Gatenby and R. J. Gillies, *Cancer Res.*, 2013, **73**, 1524.
- 13 R. A. Gatenby and E. T. Gawlinski, *Cancer Res.*, 1996, **56**, 5745.
- 14 R. A. Gatenby and R. J. Gillies, *Nat. Rev. Cancer*, 2004, **4**, 891.
- 15 O. Warburg, *Science*, 1956, **123**, 309.
- 16 I. F. Robey, B. K. Baggett, N. D. Kirkpatrick, D. J. Roe, J. Dosesco, B. F. Sloane, A. I. Hashim, D. L. Morse, N. Raghunand, R. A. Gatenby and R. J. Gillies, *Cancer Res.*, 2009, **69**, 2260.
- 17 E. A. Mazzio, B. Smith and K. F. Soliman, *Cell Biol. Toxicol.*, 2010, **26**, 177.
- 18 J. Yun, C. Rago, I. Cheong, R. Pagliarini, P. Angenendt, H. Rajagopalan, K. Schmidt, J. K. Willson, S. Markowitz, S. Zhou, L. A. Diaz, Jr., V. E. Velculescu, C. Lengauer, K. W. Kinzler, B. Vogelstein and N. Papadopoulos, *Science*, 2009, **325**, 1555.
- 19 T. Amann and C. Hellerbrand, *Expert Opin. Ther. Targets*, 2009, **13**, 1411.

- 20 R. Le Floch, J. Chiche, I. Marchiq, T. Naiken, K. Ilc, C. M. Murray, S. E. Critchlow, D. Roux, M. P. Simon and J. Pouyssegur, *Proc. Natl. Acad. Sci. U. S. A.*, 2011, **108**, 16663.
- 21 J. Chiche, K. Ilc, J. Laferriere, E. Trottier, F. Dayan, N. M. Mazure, M. C. Brahimi-Horn and J. Pouyssegur, *Cancer Res.*, 2009, **69**, 358.
- 22 R. A. Cardone, V. Casavola and S. J. Reshkin, *Nat. Rev. Cancer*, 2005, **5**, 786.
- 23 E. Bullitt, G. Gerig, S. Aylward, S. Joshi, K. Smith, M. Ewend and W. L. Lin, in *Medical Image Computing and Computer-Assisted Intervention - Miccai 2003, Pt 1*, eds. R. Ellis and T. Peters, Springer Berlin Heidelberg, 2003, vol. 2878, pp. 671.
- 24 D. Fukumura and R. K. Jain, *Microvasc. Res.*, 2007, **74**, 72.
- 25 L. Wang, X. Zhu, C. Xie, N. Ding, X. F. Weng, W. Y. Lu, X. B. Wei and C. Li, *Chem. Commun.*, 2012, **48**, 11677.
- 26 L. Wang, Z. Fan, J. Zhang, Y. Changyi, C. Huang, Y. Gu, Z. Xu, Z. Tang, W. Lu, X. Wei and C. Li, *Int. J. Cancer*, 2015, **136**, E107.
- 27 R. Khairutdinov and N. Serpone, *J. Phys. Chem. B*, 1997, **101**, 2602.
- 28 Z. Li, Y. Song, Y. Yang, L. Yang, X. Huang, J. Han and S. Han, *Chem. Sci.*, 2012, **3**, 2941.
- 29 V. R. Sheth, Y. G. Li, L. Q. Chen, C. M. Howison, C. A. Flask and M. D. Pagel, *Magn. Reson. Med.*, 2012, **67**, 760.
- 30 D. D. Castelli, G. Ferrauto, J. C. Cutrin, E. Terreno and S. Aime, *Magn. Reson. Med.*, 2014, **71**, 326.
- 31 S. Luo, E. Zhang, Y. Su, T. Cheng and C. Shi, *Biomaterials*, 2011, **32**, 7127.
- 32 C. Li, J. Xia, X. Wei, H. Yan, Z. Si and S. Ju, *Adv. Funct. Mater.*, 2010, **20**, 2222.
- 33 C. Li, K. Li, H. Yan, G. Li, J. Xia and X. Wei, *Chem. Commun.*, 2010, **46**, 1326.
- 34 Z. Si, C. Huang, X. Gao and C. Li, *RSC Adv*, 2014, **4**, 55548.
- 35 H. F. Zhang, K. Maslov, G. Stoica and L. V. Wang, *Nat. Biotechnol.*, 2006, **24**, 848.
- 36 X. D. Wang, Y. J. Pang, G. Ku, X. Y. Xie, G. Stoica and L. H. V. Wang, *Nat. Biotechnol.*, 2003, **21**, 803.
- 37 G. Ku and L. V. Wang, *Opt. Lett.*, 2005, **30**, 507.
- 38 M. G. Vander Heiden, L. C. Cantley and C. B. Thompson, *Science*, 2009, **324**, 1029.
- 39 G. Di Chiro, R. L. DeLaPaz, R. A. Brooks, L. Sokoloff, P. L. Kornblith, B. H. Smith, N. J. Patronas, C. V. Kufta, R. M. Kessler, G. S. Johnston, R. G. Manning and A. P. Wolf, *Neurology*, 1982, **32**, 1323.
- 40 M. A. Lodge, J. D. Lucas, P. K. Marsden, B. F. Cronin, M. J. O'Doherty and M. A. Smith, *Eur. J. Nucl. Med.*, 1999, **26**, 22.
- 41 D. W. Siemann, *Cancer Treat. Rev.*, 2011, **37**, 63.
- 42 E. Bullitt, D. L. Zeng, G. Gerig, S. Aylward, S. Joshi, J. K. Smith, W. L. Lin and M. G. Ewend, *Acad. Radiol.*, 2005, **12**, 1232.
- 43 A. P. Pathak, E. Kim, J. Zhang and M. V. Jones, *PloS one*, 2011, **6**, e22643.
- 44 G. Ku, X. D. Wang, X. Y. Xie, G. Stoica and L. H. V. Wang, *Appl. Opt.*, 2005, **44**, 770.
- 45 Y. Yuan, S. H. Yang and D. Xing, *Appl. Phys. Lett.*, 2012, **100**.
- 46 R. T. Tong, Y. Boucher, S. V. Kozin, F. Winkler, D. J. Hicklin and R. K. Jain, *Cancer Res.*, 2004, **64**, 3731.
- 47 V. Miranda-Goncalves, M. Honavar, C. Pinheiro, O. Martinho, M. M. Pires, C. Pinheiro, M. Cordeiro, G. Bebiano, P. Costa, I. Palmeirim, R. M. Reis and F. Baltazar, *Neuro Oncol.*, 2013, **15**, 172.